MIT Open Access Articles

Design and Manufacturing of a High-Specific-Power Electric Machine for Aircraft Propulsion

Massachusetts Institute of Technology

Design and Manufacturing of a High-Specific-Power Electric Machine for Aircraft Propulsion

Henry Andersen*, Yuankang Chen†, Mohammad M. Qasim‡, David G. Cuadrado§, David M. Otten¶, Edward Greitzer‖,
David J. Perreault**, James L. Kirtley, Jr.††, Jeffrey H. Lang‡‡, and Zoltán Spakovszky§§
Massachusetts Institute of Technology, Gas Turbine Laboratory, Cambridge, MA, 02139

Marc Amato¶¶
Innova-Logic LLC, Saunderstown, RI, 02874

This paper presents the detailed design and manufacturing of a 1-MW, air-cooled, outer-rotor, Halbach-array PMSM for aircraft propulsion. Component level risk mitigation experiments have validated the highest risk elements of the design including stator core loss, structural stability, winding insulation, and permanent magnet field strength. Two manufacturing processes for Fe-Co-V stator cores are compared through core loss and B-H curve measurements. A conventional lamination bonding process is shown to increase core loss by 20%. A novel approach to modelling Halbach array rotors is introduced and validated with experimental data and FEA. A modular single-phase winding pattern is introduced to improve robustness and enable single phase inverter drives. Full power testing is planned using two prototype machines connected through one shaft, with one acting as a motor and the other as a generator.

I. Introduction

Although batteries currently lack the energy density required to power the commercial airliners responsible for 95% of airplane CO_2 emissions, partially electrified aircraft designs, such as the NASA STARC-ABL, offer promising improvements in fuel efficiency [1, 2]. In order to realize large scale electric aircraft, megawatt-class electric machinery with a specific power exceeding 13 kW/kg is necessary [2]. Several other projects are developing high specific power, megawatt-class electric machines through scaled down 200-300 kW demonstrators [3–5]. The 1 MW electric machine presented in this paper is designed to achieve a specific power of 17 kw/kg.

Two full scale prototypes of the electric machine presented in this paper are currently being manufactured for full power demonstration at MIT. All of the major electric machine components, such as the stator cores, rotors, and heat exchangers, have been successfully manufactured. The outstanding items, such as machining the superstructure and winding the stator cores, are in progress. The prototype machines will first be tested at full operational speed (12,500 RPM) with no load connected to the shaft. To demonstrate the design at full power, the two prototype machines will be connected through a shaft, with one machine operating as a motor and the other as a generator.

During the manufacturing process of the 1 MW demonstrator, the highest risk aspects of the design have been validated through stator core loss experiments (Sec. 3B), winding and insulation tests (Sec. 4), rotor spin-pit testing at full operational speed and temperature (Sec. 5B), and rotor magnetic field measurements (Sec. 5C). Experimental results indicate that the demonstrator will meet the design specifications and achieve full power. More information on the thermal management system, rotordynamic design, and power electronics drive is published in [6–8] respectively.

---

*Graduate Research Assistant, EECS, 31-304

†Doctoral Candidate, AeroAstro, 31-304D

‡Doctoral Candidate, EECS, 10-026

§Research Engineer, 31-316

¶Principal Research Engineer, Research Laboratory of Electronics, 10-039

‖H.N. Slater Professor of Aeronautics and Astronautics, 31-319

**Ford Foundation Professor of Engineering, 10-039

††Professor of Electrical Engineering (Post-Tenure), 10-098

‡‡Vitesse Professor of Electrical Engineering, 10-176

§§T. A. Wilson Professor of Aeronautics and Astronautics; Head, Air Sector; Director, Gas Turbine Laboratory, 31-317
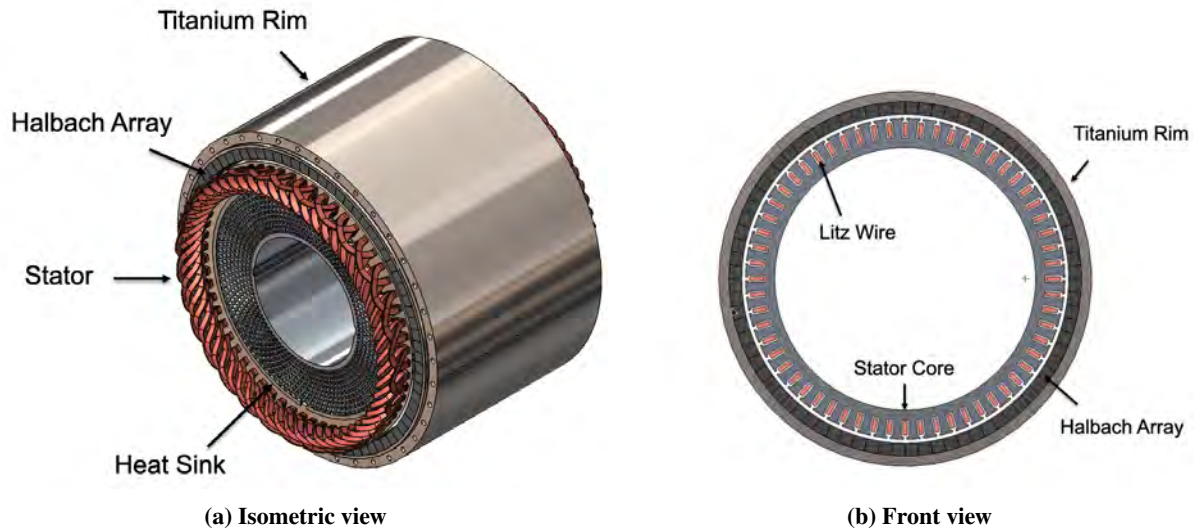
¶¶CEO

1

(a) Isometric view   **(b) Front view**

Fig. 1   High power density electric machine for turboelectric propulsion

II. Overview of Electric Machine Design

A trade-space analysis of electric machine architectures found that the outer rotor, radial flux, permanent magnet synchronous machine (PMSM) achieves the optimal combination of power density and thermal manageability for aircraft propulsion [9, 10]. The outer rotor architecture and air cooled thermal management system enable the machine to be directly integrated inside of a turbomachine as a generator. An integrated prime mover concept using this electric machine is proposed in [9]. Fundamental design details such as geometry, speed, torque, and pole count were co-optimized considering the structural feasibility, weight, and efficiency the electric machine, the thermal management system, and the power electronics drive [9–11].

A structural view of the electric machine is shown in Figure 1. The key metrics of the design are presented in Table 1. The Halbach array rotor eliminates the need for rotor back iron. Instead, a light-weight titanium rim is used to retain the permanent magnets. Within the Halbach array, the use of four directions of magnetization per pole decreases the harmonic distortion of the airgap flux density and reduces torque ripple to 1% of the average torque. 0.1 mm Iron-Cobalt stator laminations and Litz wire mitigate core loss and ohmic loss at the high operational electrical frequency. A modular, single-phase winding pattern improves reliability and enables single-phase inverter drives [6]. A novel, channel-type heat sink enables air-cooling at full power [6].

2

Table 1 Electric Machine Design Specifications

Metric		Value	Units
Power		1	MW
Specific Power		17	kW/kg
Speed		12,500	RPM
Shear stress		5.3	PSI
Efficiency		97.3 %	-
Slot current density (peak)		13.3	A/mm^2
Number of pole pairs / slots		10 / 60	-
Size	Stack length	198	mm
	Outer diameter	300	mm
	Air gap	3	mm
Material	Stator core	Vacodur 49, 0.1 mm	Fe-Co-V
	Winding	Litz Type 8	Cu
	Permanent magnet	Recoma® 35E	Sm-Co
	Retaining sleeve	Titanium	Ti

Figure 2 shows the expected loss of the electric machine. Stator core loss is calculated through FEA using experimental data (Sec. 3B). Permanent magnet loss is calculated through FEA using material data provided by the vendor. The ohmic and windage losses are calculated with models described in [9] and [10] respectively. The specific power of the electric machine is calculated using the mass in Table 2. Superstructure and bearing system masses are not included in the specific power calculation because they would change depending on the application of the machine, and therefore they are not optimized for specific power.

Fig. 2 Breakdown of electric machine loss

Table 2 Breakdown of electric machine mass

Component	Mass [kg]
Stator Core	19.7
Windings	6.1
Magnets	14.6
Rim	10.6
Heat sink	6.4
Total	**57.4**

III. Low Loss Stator

Stator core loss is the dominate component of loss in the electric machine design [9]. Mitigating stator core loss is essential to building megawatt-class electric machines that operate at electrical frequencies in excess of 1000 Hz. The stator core loss is estimated through FEA using experimental data collected on material samples.

Stator core loss is notoriously difficult to predict, as the mechanism is not fully understood. FEA core loss calculations often rely on extrapolating experimental data beyond the highest frequency available to account for the impact of higher order harmonics. Additionally, the effects of rotating magnetic fields and stress imposed by the manufacturing process of the stator core are not usually replicated in experimentally measured data provided by the material vendor [12, 13]. As a result, the measured core loss can reach as high as twice the estimated loss [14].

The stator core loss estimate is multiplied by a safety factor of 2 to account for the unreliability of the core loss prediction. Additionally, the core loss estimate uses experimental data measured on the core material after the manufacturing process (Sec. 3A). Including the core loss safety factor of 2 in the co-optimizer lowered the rotational speed of the optimized machine by 20% [9]. Once experimental results of the machine at full power are available, the safety factor for stator core loss can be updated for recommendation to future designs.

The stator back iron and tooth width are sized to minimize magnetic saturation, subject to a tradeoff between mass, core loss, and current density in the slot section. Saturation increases the harmonic distortion of the stator flux density waveform, which increases core loss and causes undesirable nonlinear magnetic behavior. However, increasing the size of stator core to reduce saturation increases mass and increases loss for a fixed current. The stator operates with a peak flux density of 2.2 T.
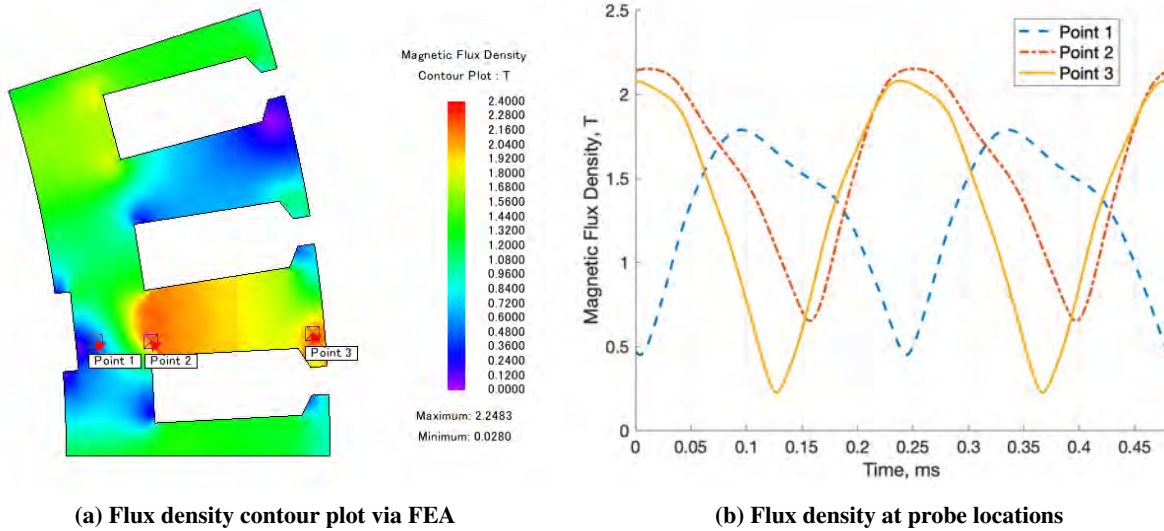

(a) Flux density contour plot via FEA   (b) Flux density at probe locations

Fig. 3   Flux density in stator via FEA

4

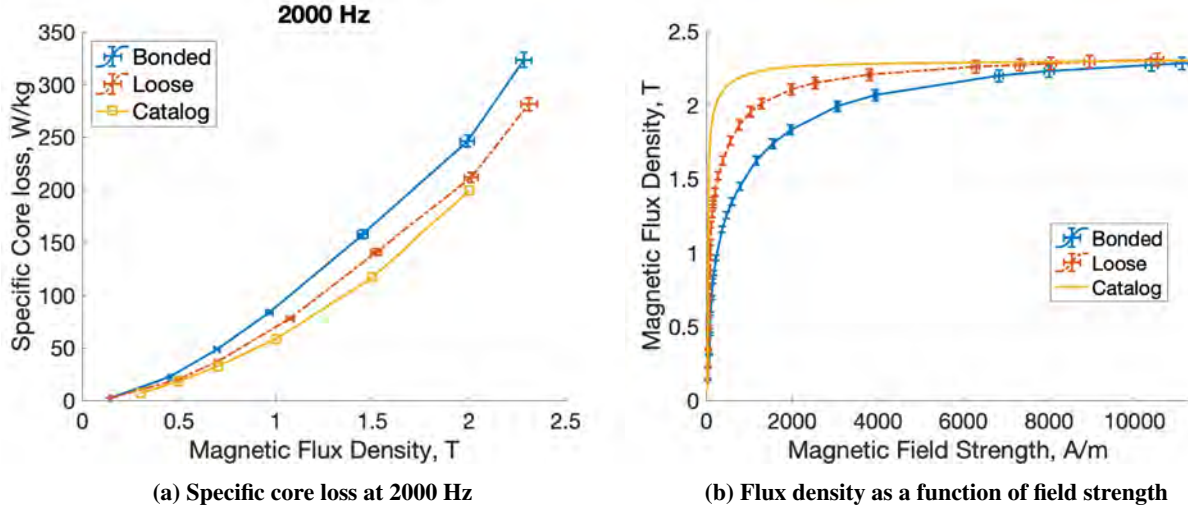| (a) Specific core loss at 2000 Hz	(b) Flux density as a function of field strength

Fig. 4   Magnetic properties of 0.1 mm Vacoflux 48 (Fe-Co-V) laminations before and after bonding

A. Stator Manufacturing

An Iron-Cobalt-Vanadium alloy with 0.1 mm thick laminations is selected to achieve high saturation flux density (2.2 T) and low core loss. Using 0.15 mm laminations results in core loss that exceeds the limit of the thermal management system. Iron-cobalt alloys are particularly susceptible to the magnetostriction effect, which causes permeability to decrease and core loss to increase as mechanical stress increases [15]. A conventional lamination bonding process was found, experimentally, to increase measured core loss by 20%, as opposed to unbonded (loose) laminations (Fig. 4a). Section 3B discusses the details of the experimental setup. For thicker laminations, the effect of bonding on core loss would likely decrease.

To avoid mechanically stressing the stator core laminations, Manufacturing Process #1 was developed (Fig. 5). Photochemical etching was selected to impart less edge trauma than standard alternatives such as stamping or laser cutting. However, the stator core manufactured by Process #1 incurred significant delays due partially to the time spent shipping the laminations between five separate vendors. While pursuing Process #1, Process #2 became available as an alternative. The stator core manufactured through Process #2 arrived in significantly less time than the stator core manufactured through Process #1. The two stator cores are shown in Figure 6.
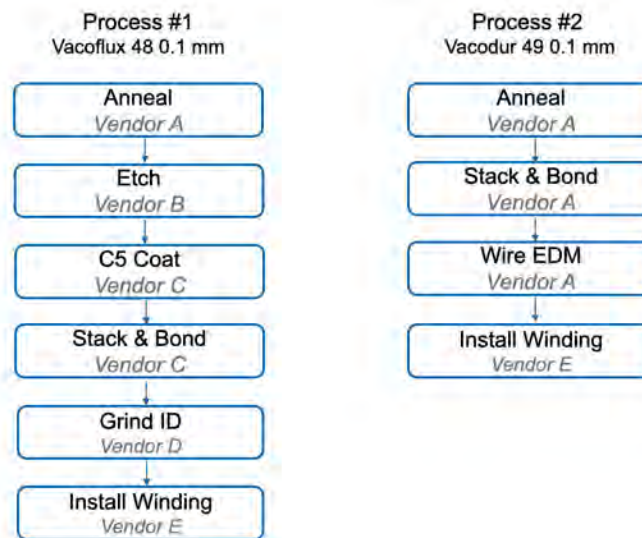

Fig. 5   Two different manufacturing processes for stator core

Fig. 6 Manufactured two stator cores with different processes

The magnetic properties of the cores manufactured through Process #1 and Process #2 were experimentally characterized; see Figure 7. Process #2 achieves lower core loss and higher permeability than Process #1 . The machine is simulated in FEA using the experimentally measured B-H curves of cores from Process #1 and Process #2. Process #2 results in 1% higher torque and 0.1 T higher peak flux density than Process #1 (Fig. 8). Process #2 is recommended for manufacturing future stator cores over Process #1. However, both stator cores will be used in the 1-MW demonstrator described in Section 6B, as both cores are expected to meet the design requirements.
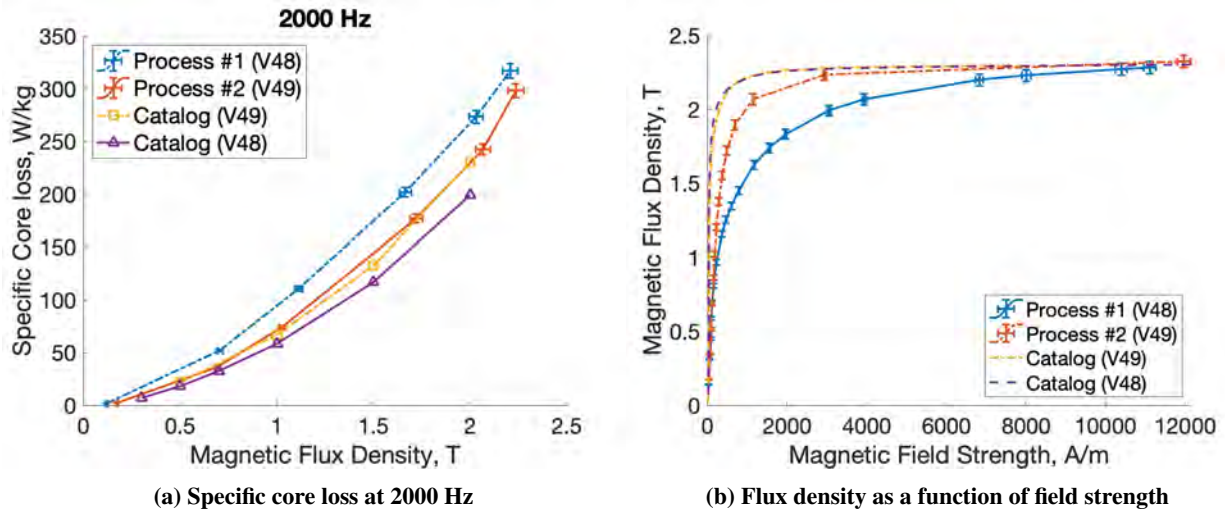

(a) Specific core loss at 2000 Hz

(b) Flux density as a function of field strength

Fig. 7 Magnetic properties of Fe-Co-V alloys "Vacoflux 48" and "Vacodur 49" with different manufacturing processes
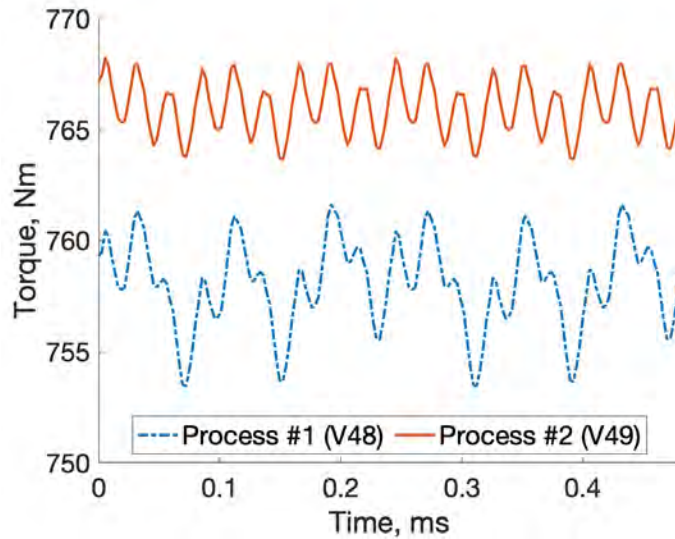
Fig. 8   Torque via FEA using experimental data of different materials

B. Magnetic Material Characterization

Specific core loss and B-H curves are measured for different materials and manufacturing processes using 40 mm diameter toroidal samples. The samples are wound with 90 primary turns and 30 secondary turns. A sinusoidal voltage amplifier drives the primary winding. An oscilloscope measures the voltage on the secondary coil winding and the current in the primary winding. The voltage on the secondary winding is only due to induction, because no current flows through the secondary winding.
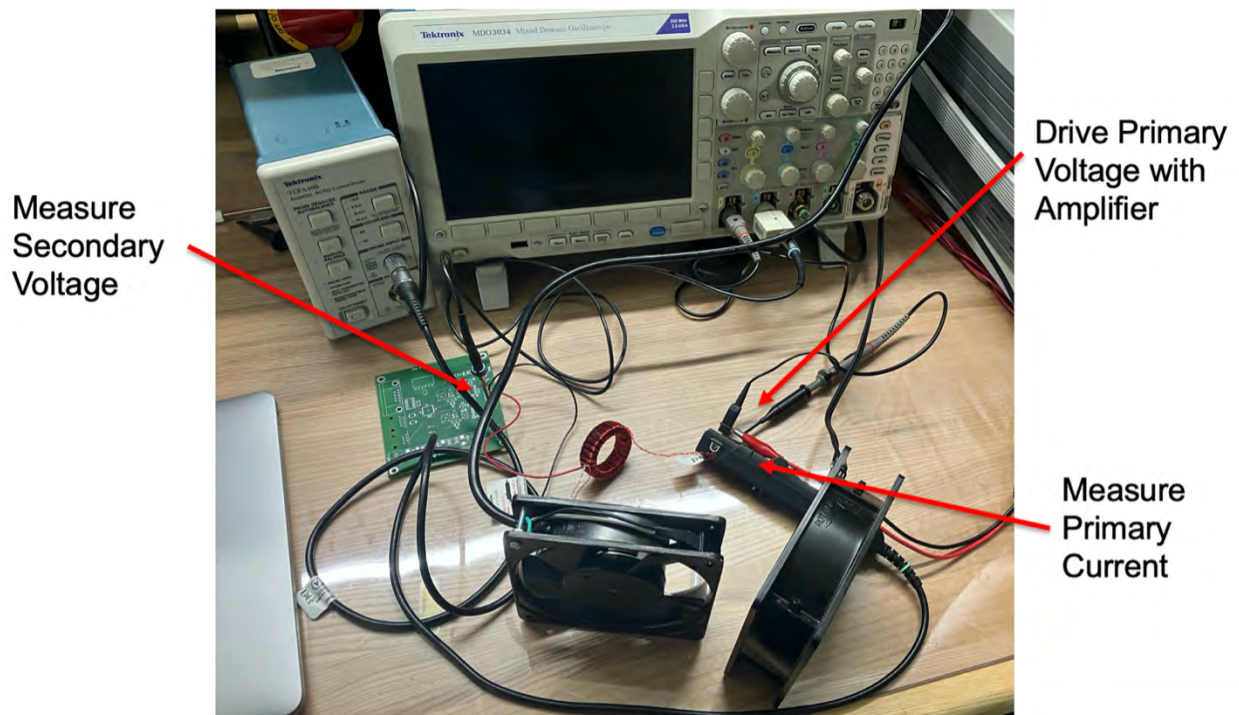

Fig. 9   Experiment Setup for Characterizing Magnetic Materials

The magnetic field strength (H), flux density (B), and specific core loss ($\frac{P_c}{m_c}$) are calculated with

$$H = \frac{N_1 * I_1}{l_c} \tag{1}$$

$$B = \frac{1}{N_2 * A_c} \int V_2(t)\, dt \tag{2}$$

$$\frac{P_c}{m_c} = \frac{1}{m_c * T} \int_0^T I_1 * \frac{N_1}{N_2} V_2(t)\, dt, \tag{3}$$

where I_1 is primary current; V_2 is secondary voltage; N_1, N_2 are number of primary and secondary turns respectively; A_c is cross sectional area of core; l_c is mean core length; m_c is mass of core; and T is period.

In some cases, the core loss of a stator stack can be measured directly instead of using smaller toroid samples [16]. However, an amplifier capable of supplying sufficient power to test the full stator at 2,000 Hz was unavailable. Instead, the core loss and B-H curve of a 0.5 inch bonded stack of full-size stator laminations was measured to ensure the data from the toroidal samples will match the full size stator. A mechanical natural frequency of the shortened stator stack was excited at 2 kHz, causing excessive vibrations to disrupt the measurement. At 2.5 kHz, the core loss of the partial stator stack closely matches the core loss of the smaller toroidal samples (Fig. 12).
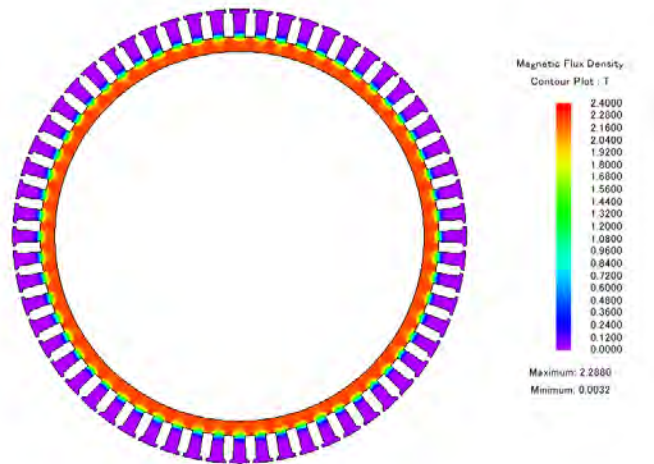

Fig. 10   Partial stator stack

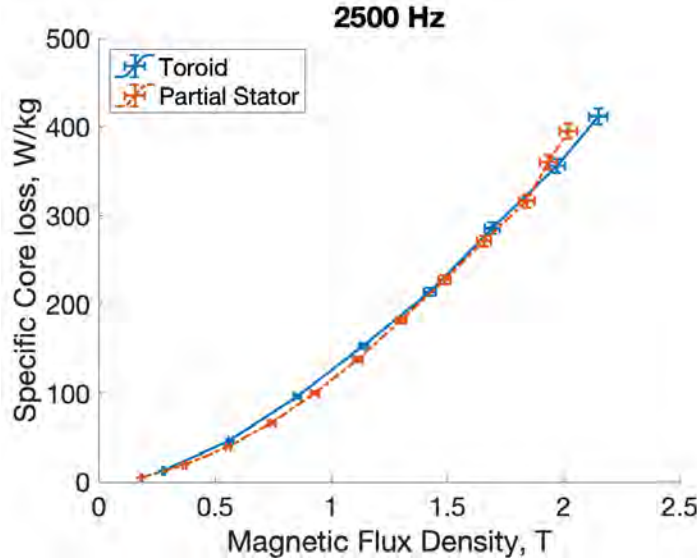Fig. 11   Flux density in partial stator experiment via FEA

8

Fig. 12   Specific core loss of 200 mm diameter partial stator matches 40 mm diameter toroid

IV. Winding

The electric machine winding consists of 10 independent three-phase pole-pair windings. Modular winding schemes are increasing in popularity for electric machines designed for aviation due to their improved reliability over non-modular windings [17]. A pole pair contains 3 single phase concentrated windings driven by 3 single phase inverters. Single phase inverters are shown to improve power density and robustness for the present application in [18].

Rectangular Type 8 (US AWG 24) Litz bundles [19] are used to minimize AC winding losses and maximize copper fill factor. Kapton® tape and Nomex® slot liners are placed between phase windings in the slots and the end turns to improve phase to phase insulation. The slots are Vacuum Pressure Impregnated (VPI) with CoolTherm® EP-2000 epoxy to improve thermal conductivity and electrical insulation [20]. CoolTherm® EP-2000 offers favorable dynamic viscosity, improving the penetration of the varnish during the VPI process [10].

A mockup, single-pole-pair section of the stator was manufactured to verify the winding process. The stator section withstood full operational voltage and current without insulation failure [8]. The stator section successfully demonstrated the winding pattern, insulation, and thermal sensor installation.
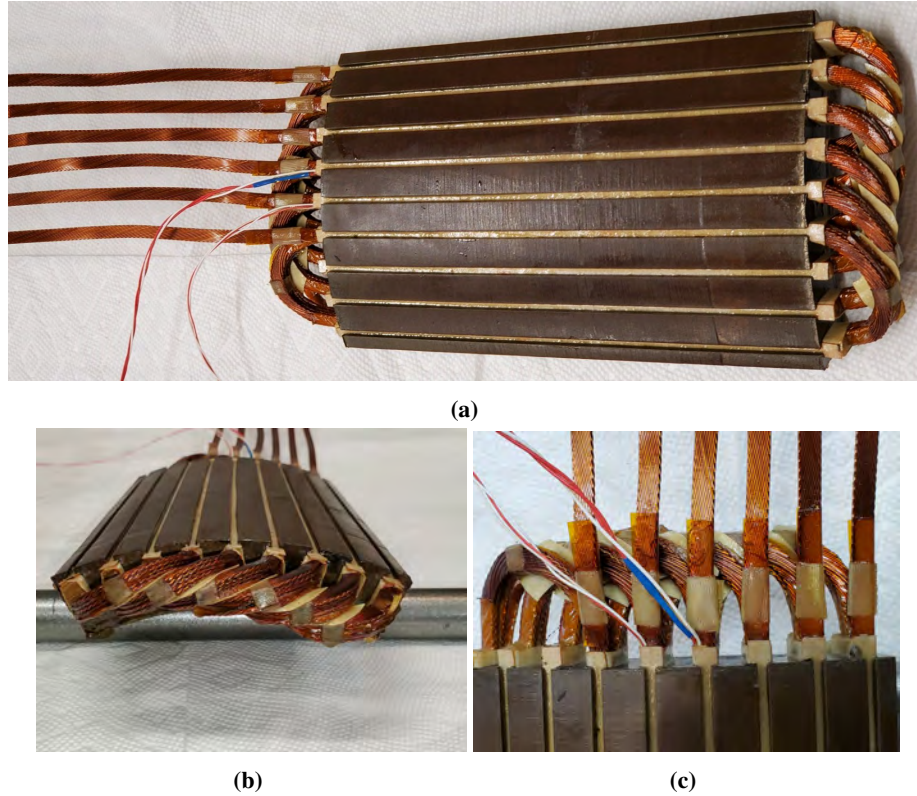
9

Fig. 13 **Single-pole-pair stator section to verify winding process (a) Top view (b) Side view (c) Zoomed in**

V. Halbach Array Rotor

The electric machine is expected to achieve 1% torque ripple through the use of a permanent-magnet, Halbach-array rotor with four directions of magnetization per pole. The Halbach array creates nearly sinusoidal air gap flux density, eliminating the need for rotor back iron. Instead, a titanium rim retains the magnets.

A. Halbach Array Model

The model described in this section describes how the number of tangential segments in a Halbach array rotor, N_h, impacts torque and air gap flux density. The model provides a powerful alternative to FEA to reduce to burden of computation during the design process. The model differs from existing models [21–23] by replacing the magnetization vector ($\vec{M}$) with a combination of magnetic surface charges and currents that reside only on the inner - and outer - radius surfaces of the magnet array; see Figure 15. As a result, the model is simple, easy to use, and easy to adapt to different machine topologies.
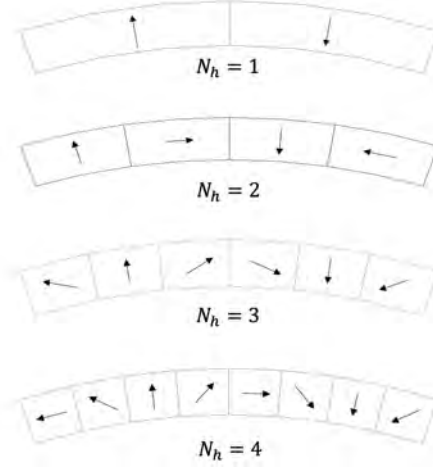
Fig. 14 Halbach arrays with various numbers of directions of magnetization per pole (N_h)
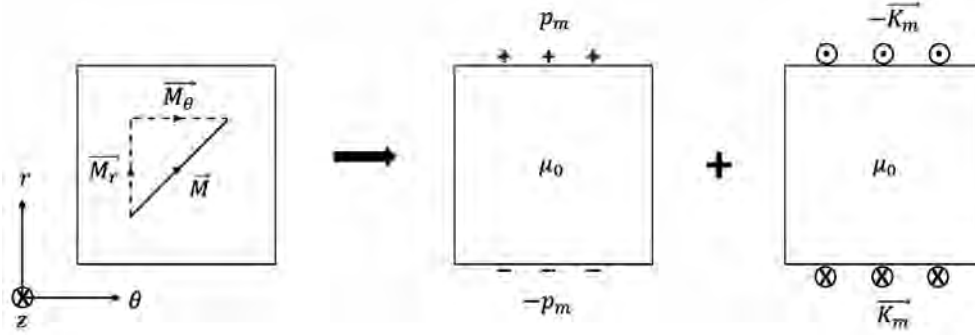

Fig. 15 M_r is replaced by $\pm p_m$ and M_θ is replaced by $\pm\vec{K}_m$ thereby moving the magnetization to surface sources across only two surfaces

The magnetic surface charge (p_m) and surface current in the axial direction ($K_{m,z}$) on the inner surface of the Halbach array are expressed as Fourier series,

$$K_{m,z} = \sum_n K_n \cos(np\theta) \qquad p_m = \sum_n p_n \sin(np\theta) \qquad (4)$$

$$K_n = \frac{2}{\pi}M_0 \sum_{i=0}^{N_h} \frac{1}{n}\cos(\frac{\pi i}{N_h})[\sin(np\theta_{b,i})-\sin(np\theta_{a,i})] \qquad p_n = \frac{2}{\pi}M_0 \sum_{i=0}^{N_h} \frac{1}{n}\sin(\frac{\pi i}{N_h})[\cos(np\theta_{a,i})-\cos(np\theta_{b,i})] \quad (5)$$

- For odd number of magnetizations per pole (e.g. $N_h = 1, 3, 5, ..$)

$$\theta_{a,i} = \frac{\pi i}{pN_h} \qquad \theta_{b,i} = \frac{\pi(i+1)}{pN_h} \qquad (6)$$

- For even number of magnetizations per pole (e.g. $N_h = 2, 4, 6, ..$)

$$\theta_{a,i} = \max(\frac{\pi(i-0.5)}{pN_h}, 0) \qquad \theta_{b,i} = \min(\frac{\pi(i-0.5)}{pN_h}, \frac{\pi}{p}), \qquad (7)$$

where p is the number of pole pairs; $M_0 = \frac{B_r}{\mu_0}$; B_r is remnant magnetic flux density; and N_h is number of directions of magnetization per pole (Fig. 14).

(a) Magnetic surface charge
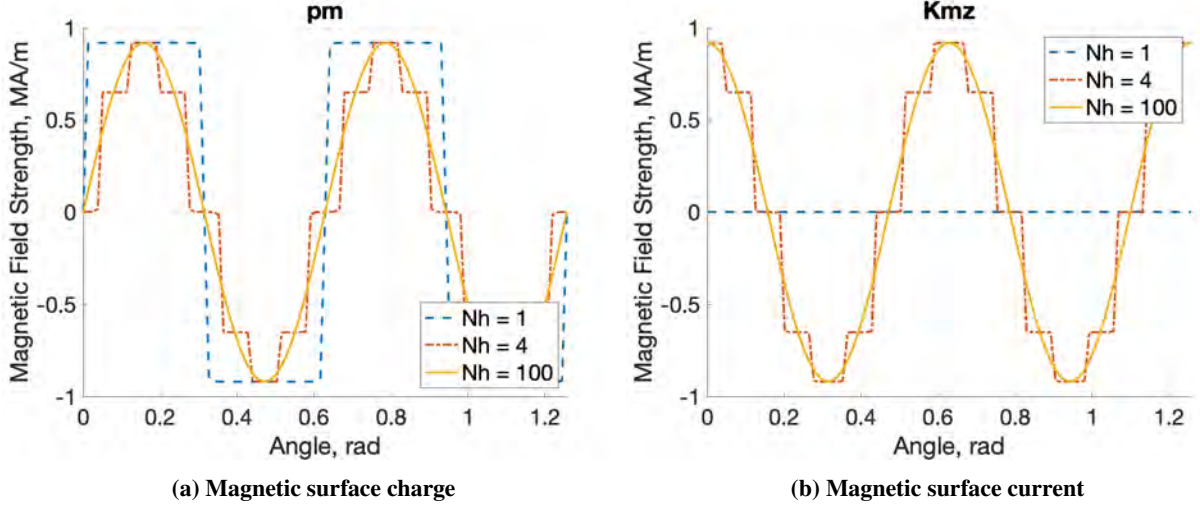
(b) Magnetic surface current

Fig. 16 Magnetic surface current and charge for various numbers of directions of magnetization per pole, N_h

The magnetic field in the airgap is dermined by first solving Maxwell's equations driven by the boundary conditions from both p_m and $K_{m,z}$ on the inner surface of the Halbach array. The same approach is repeated using the boundary conditions from both magnetic surface charge and current on the outer surface. Magnetic surface charge and current on the outer surface of the Halbach array are simply the opposite of those on the inner surface. The two fields are superimposed to find the total magnetic field in the airgap.

For the outer rotor, inner stator machine, the resulting boundary value problems are depicted in Fig. 17. At the surface of the stator, $r = R_s$, the tangential magnetic field disappears and the radial magnetic field is given by

$$H_{r,rotor}(\theta, r = R_s) = \sum_n (p_n + K_n) \left[\left(\frac{R_s}{R_{ro}} \right)^{np-1} - \left(\frac{R_s}{R_{ri}} \right)^{np-1} \right] \sin(np\theta), \qquad (8)$$

where R_{ro} is the outer radius of the rotor magnets, and R_{ri} is the inner radius of the rotor magnets.

Eq. (8) shows that the magnetic field in the air gap becomes less harmonically distorted as the number of Halbach segments N_h increases and p_m and $K_{m,z}$ become more sinusoidal (Fig. 16). The magnetic field from the model closely matches experimental data and FEA (Fig. 20a).
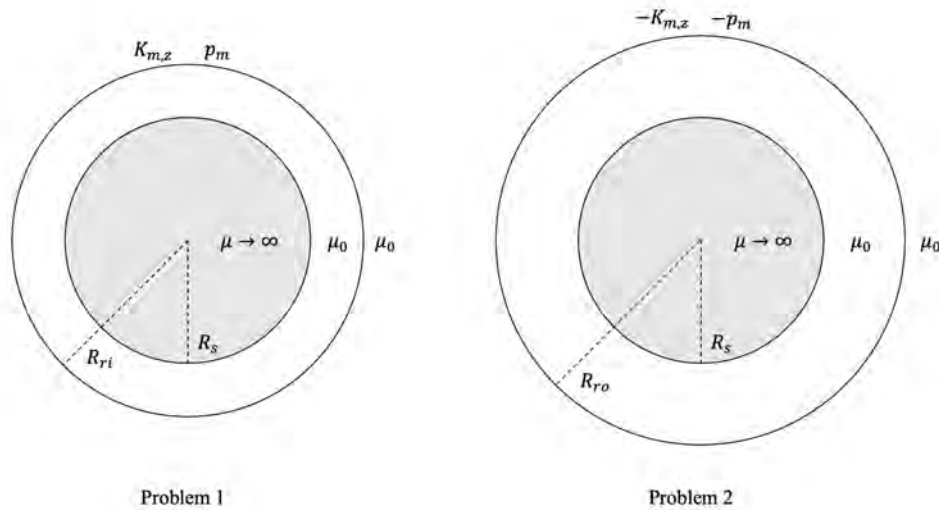

Problem 1

Problem 2

Fig. 17 Boundary value problems for the outer rotor, inner stator machine
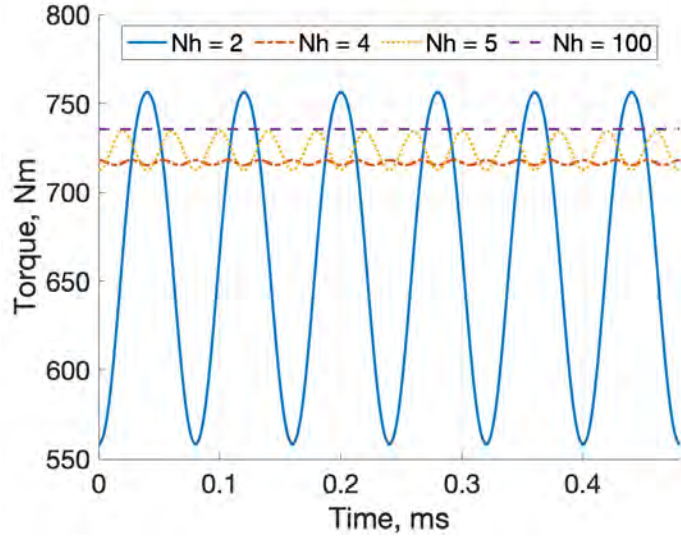
12

Fig. 18   Torque from the stress tensor for various numbers of directions of magnetization per pole, N_h

Torque is calculated using the Maxwell stress tensor on the Halbach array field in Eq. (8) and the stator field model described in [9, 24],

$$T = \mu_0 L R_s^2 \int_0^{2\pi} H_{\theta,stator} H_{r,rotor} \, d\theta \tag{9}$$

$$T = \mu_0 \pi L R_s^2 \left[\sum_{n=1,7,13...} A_n B_n \cos(\omega_e t(1-n)) + \sum_{n=5,11,17...} A_n B_n \cos(-\omega_e t(1+n)) \right] \tag{10}$$

$$A_n = -\frac{3}{n\pi} \frac{I_{pk}}{w_{so}} \left[\cos(\frac{n\pi}{2} - np\frac{w_{so}}{2R_s}) - \cos(\frac{n\pi}{2} + np\frac{w_{so}}{2R_s}) \right] \tag{11}$$

$$B_n = (p_n + K_n) \left[\left(\frac{R_s}{R_{ro}} \right)^{np-1} - \left(\frac{R_s}{R_{ri}} \right)^{np-1} \right], \tag{12}$$

where L is the axial length of the machine; I_{pk} is the peak current in the stator windings; and w_{so} is the width of the stator slot openings.

The torque expression reveals how average torque and torque ripple depend on machine geometry (R_s, R_{ri}, R_{ro}, w_{so}, l), the number of directions of magnetization per pole (p_n, K_n), stator current (I_{pk}), permanent magnet strength (p_n, K_n), and the number of pole pairs (p). As the number of directions of magnetization per pole (N_h) increases, the average torque increases (Fig. 18) and the torque ripple generally decreases except from $N_h = 4$ to $N_h = 5$.

As N_h increases, the Halbach array rotor becomes more difficult to manufacture because the magnet segments are thinner tangentially and the magnets have unusual angles of magnetization. Four directions of magnetization per pole was selected for the electric machine as a compromise between performance and manufacturability based on vendor feedback.

The Halbach array model described above significantly reduces the burden of computation from FEA during the design process. The model produces 5% lower average torque and peak flux airgap density than FEA (Figs. 8, 17, 20a), on par with alternative Halbach array models [21, 22]. The model is easy to use and adapt to different machine topologies.

B. Rotor Manufacturing

Recoma® 35E Sm-Co magnets are used in the Halbach array rotor. They offer superior temperature stability over alternative Nd-B-Fe magnets [25]. The rotor is magnetized at angles in increments of 45°, with 4 tangential segments

Fig. 19   Halbach array rotor was successfully manufactured

per pole (Fig. 14). The magnets are axially segmented into 64, 3.1 mm segments, reducing permanent magnet loss to 20% of the unsegmented value [9].

The Halbach array rotor has been successfully manufactured (Fig. 19). The rotor was spun at full operational speed (12,500 RPM) and temperature in a "spin pit". During spin pit testing, the vibration levels remained within tolerance. Balance measurements of the rotor met the G 2.5 specification before and after spin pit testing. More information on the rotordynamic design of the electric machine is provided in [7].

C. Rotor Field Strength Test

The magnetic field strength of the rotor was measured at 1.5 mm from the inner surface of the magnet array. The field scan data closely aligns with FEA data and the model described in section 5A in the absence of a stator (Fig. 20a). The field scan data is consistent across all pole pairs and the full axial length of the rotor (Fig. 20b). The field scan data suggests that the prototype machine should achieve the full rated torque predicted by FEA if the stator operates as expected (Fig. 8).
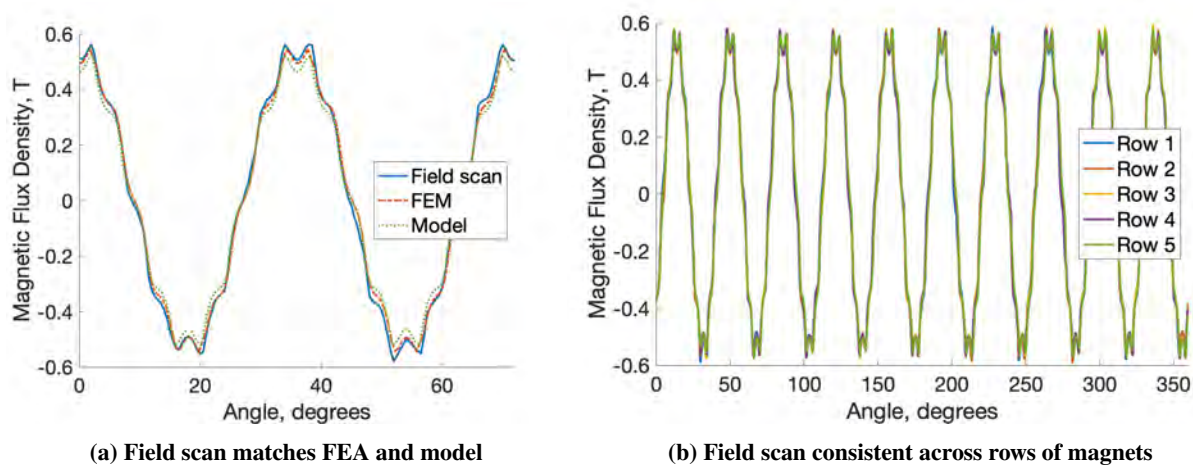

(a) Field scan matches FEA and model

(b) Field scan consistent across rows of magnets

Fig. 20   Rotor field scan data

VI. Planned Experiments

The highest risk aspects of the electric machine design have been verified through the core loss experiments (Sec. 3B), the insulation and winding process test (Sec. 4), the spin pit test (Sec. 5B), and the rotor magnetic field measurement (Sec. 5C). The experimental results indicate that the demonstrator machine will meet the design specifications and achieve full power. The major electric machine components for two prototype machines, such as the stator cores, rotors, and heat sinks, have all been successfully manufactured. The remaining tasks, such as machining the superstructure and winding the stator cores, are currently in progress. Experimental validation of the electric machine will begin once manufacturing and assembly of the first machine is completed.

A. No Load, Full Speed Test

The first prototype machine will be tested at full operational speed (12,500 RPM), with no load connected to the shaft. A 150 kW DC supply will power the machine. An absolute shaft encoder will be used for control. The no load test will quantify how well the back-EMF matches FEA prediction. The no load test will demonstrate rotordynamic stability of the machine and verify that the controller and instrumentation operate as expected. A spin down test will yield the total rotating loss at different speeds, from which the core loss will be estimated.

B. Full Power Test

To test the electric machine at full power, two prototype electric machines will be coupled through one shaft, with one machine acting as a motor and one machine as a generator (Fig. 21). The electric power from the generator will supply the motor. Both machines will operate at full power. An external 150 kW power supply will supply the losses in the system. The superstructure and piping are designed to air-cool both electric machines and drives with forced air from an external air compressor. The superstructure and machine carry extensive instrumentation to measure temperature and vibration throughout the system. The full power test will verify the rated torque, power, and efficiency of the electric machine and demonstrate the thermal management and rotordynamic stability of the system.
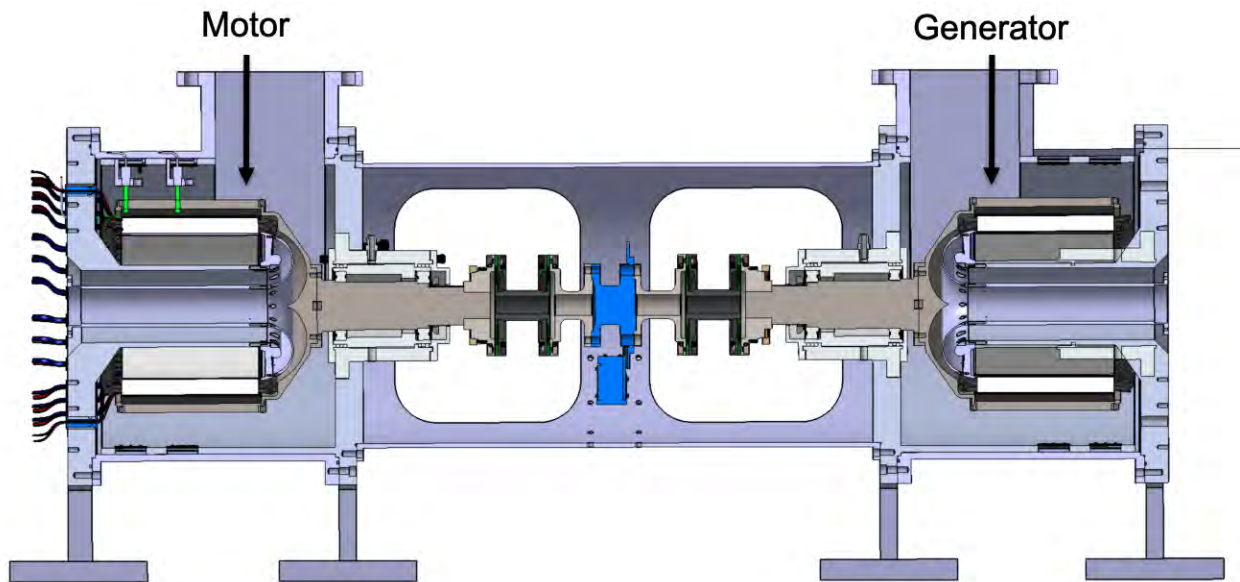

Fig. 21   Two prototype electric machines configured for full power testing

VII. Conclusion

This paper presents the detailed design and manufacturing process of a 1-MW, air-cooled, outer-rotor, Halbach-array PMSM. Component level risk mitigation experiments indicate that the performance of the prototype machine will match the design specifications.

The stator core loss estimate has been validated through experimental measurements on toroidal samples and full size stator laminations. The lamination bonding process is shown to increase the core loss of Fe-Co-V material by a factor of 1.2. Two manufacturing process for Fe-Co-V stator cores have been compared through core loss and B-H curve measurements.

A modular, single-phase winding pattern increases the robustness and power density of the system by enabling single-phase inverter drives. The stator winding process and insulation have been successfully demonstrated through a mockup stator winding.

A new model for Halbach array rotors is introduced, offering a computationally efficient alternative to FEA during the design process. The model matches FEA and experimental data within 5%. The model is simple, easy to use, and easy to adapt to different machine toplogies.

A Halbach array rotor with 4 tangential segments per pole has been manufactured and spun at full operational speed and temperature. A magnetic field scan of the rotor closely matches the analytical model and FEA, indicating that the the rated torque of the demonstrator will meet the design specification.

Testing will begin with spinning a single machine at full operational speed with no load connected to the shaft. The design will be tested at full power by coupling two prototype machines through a shaft and operating one machine as a motor and the other as a generator.

The models, manufacturing processes, and experiments presented in this paper are useful for building high speed, high specific power electric machines for applications such as electric aircraft and electric vehicles.

Acknowledgments

References

[1] Epstein, A. H., and O'Flarity, S. M., "Considerations for Reducing Aviation's CO2 with Aircraft Electric Propulsion," *Journal of Propulsion and Power*, Vol. 35, No. 3, 2019, pp. 572–582. https://doi.org/10.2514/1.B37015.

[2] Jansen, R., Bowman, C., Jankovsky, A., Dyson, R., and Felder, J., "Overview of NASA Electrified Aircraft Propulsion Research for Large Subsonic Transports," *53rd AIAA/SAE/ASEE Joint Propulsion Conference, AIAA Propulsion and Energy Forum*, 2017, pp. 8–27. URL https://ntrs.nasa.gov/archive/nasa/casi.ntrs.nasa.gov/20170012222.pdf.

[3] Swanke, J., Zeng, H., Bobba, D., Jahns, T. M., and Sarlioglu, B., "Design and Testing of a Modular High-Speed Permanent-Magnet Machine for Aerospace Propulsion," *2021 IEEE International Electric Machines Drives Conference (IEMDC)*, 2021, pp. 1–8. https://doi.org/10.1109/IEMDC47953.2021.9449536.

[4] Lee, D., Balachandran, T., Sirimanna, S., Salk, N., Yoon, A., Xiao, P., Macks, J., Yu, Y., Lin, S., Schuh, J., Powell, P., and Haran, K. S., "Detailed Design and Prototyping of a High Power Density Slotless PMSM," *IEEE Transactions on Industry Applications*, Vol. 59, No. 2, 2023, pp. 1719–1727. https://doi.org/10.1109/TIA.2022.3230379.

[5] Xu, L., Wang, H., Xiong, H., Ke, Z., Woo, J., Zhang, J., and Dong, S., "Design and Experimental Evaluation of a High Specific Power Permanent Magnet Synchronous Machine," *2019 IEEE International Electric Machines Drives Conference (IEMDC)*, 2019, pp. 1296–1302. https://doi.org/10.1109/IEMDC.2019.8785246.

[6] Chen, Y., Spakovszky, Z. S., Greitzer, E. M., Cordero, Z. C., Cuadrado, D. G., and Gump, C., "Novel Channel-type Heat Exchanger for a Megawatt-Class Integrated Motor Drive Technology Demonstrator," AIAA/IEEE Electric Aircraft Technologies Symposium (EATS), 2023. Extended Abstract Submission.

[7] Chen, Y., Spakovszky, Z. S., Greitzer, E. M., Cordero, Z. C., Cuadrado, D. G., and Amato, M., "High Speed Rotor System for a Megawatt-Class Integrated Motor Drive Technology Demonstrator," AIAA/IEEE Electric Aircraft Technologies Symposium (EATS), 2023. Extended Abstract Submission.

[8] Qasim, M. M., Otten, D. M., Spakovszky, Z. S., Lang, J. H., Kirtley, J. L., and Perreault, D. J., "Design and Optimization of an Inverter for a One-Megawatt Ultra-Light Motor Drive," AIAA/IEEE Electric Aircraft Technologies Symposium (EATS), 2023.

[9] Dowdle, A., "Design of a High Specific Power Electric Machine for Turboelectric Propulsion," Ph.D. thesis, Massachusetts Institute of Technology, 2022.

[10] Chen, Y., "Technology Demonstration of a Megawatt-Class Integrated Motor Drive for Aircraft Propulsion," Ph.D. thesis, Massachusetts Institute of Technology, 2023.

[11] Chen, Y., Spakovszky, Z. S., Greitzer, E. M., Cordero, Z. C., Lang, J. H., Kirtley, J. L., Perreault, D. J., Andersen, H. N., Qasim, M. M., Cuadrado, D. G., and Otten, D. M., "Technology Demonstration of a Megawatt-Class Integrated Motor Drive for Aircraft Propulsion," AIAA/IEEE Electric Aircraft Technologies Symposium (EATS), 2023.

[12] Alatawneh, N., and Pillay, P., "The impact of rotating field on core loss estimation in electrical machine laminations," *2012 IEEE Energy Conversion Congress and Exposition (ECCE)*, 2012, pp. 2696–2703. https://doi.org/10.1109/ECCE.2012.6342535.

[13] Ebrahimi, H., Gao, Y., Dozono, H., Muramatsu, K., Okitsu, T., and Matsuhashi, D., "Effects of Stress and Magnetostriction on Loss and Vibration Characteristics of Motor," *IEEE Transactions on Magnetics*, Vol. 52, No. 3, 2016, pp. 1–4. https://doi.org/10.1109/TMAG.2015.2493098.

[14] Tekgun, B., "Analysis, Measurement and Estimation of the Core Losses in Electrical Machines," Ph.D. thesis, The University of Akron, 2016.

[15] Moses, A., and Thomas, B., "Stress sensitivity of the A.C. magnetic properties of permendur after various heat treatments," *IEEE Transactions on Magnetics*, Vol. 12, No. 2, 1976, pp. 103–106. https://doi.org/10.1109/TMAG.1976.1059003.

[16] Cossale, M., Krings, A., Soulard, J., Boglietti, A., and Cavagnino, A., "Practical Investigations on Cobalt–Iron Laminations for Electrical Machines," *IEEE Transactions on Industry Applications*, Vol. 51, No. 4, 2015, pp. 2933–2939. https://doi.org/10.1109/TIA.2015.2394404.

[17] Zeng, H., Swanke, J., Jahns, T. M., and Sarlioglu, B., "Modular Modeling and Distributed Control of Permanent-Magnet Modular Motor Drives (MMDs) for Electric Aircraft Propulsion," *2021 IEEE Energy Conversion Congress and Exposition (ECCE)*, 2021, pp. 4598–4605. https://doi.org/10.1109/ECCE47101.2021.9594943.

[18] Qasim, M. M., Otten, D. M., Lang, J. H., Kirtley, J. L., and Perreault, D. J., "Comparison of Inverter Topologies for High-Speed Motor Drive Applications," *2021 IEEE 22nd Workshop on Control and Modelling of Power Electronics (COMPEL)*, 2021, pp. 1–8. https://doi.org/10.1109/COMPEL52922.2021.9645956.

[19] *Type 8 Litz Wire*, New England Wire Technologies, 2023. URL https://litzwire.com/types-of-litz-wire/type-8-litz-wire/.

[20] *CoolTherm EP-2000*, Parker / Lord, 2023. URL https://files.lord.com/pdf/44/DS4323_CoolThermEP-2000.pdf.

[21] Song, Z., Liu, C., Feng, K., Zhao, H., and Yu, J., "Field Prediction and Validation of a Slotless Segmented-Halbach Permanent Magnet Synchronous Machine for More Electric Aircraft," *IEEE Transactions on Transportation Electrification*, Vol. 6, No. 4, 2020, pp. 1577–1591. https://doi.org/10.1109/TTE.2020.2982733.

[22] Xia, Z., Zhu, Z., and Howe, D., "Analytical magnetic field analysis of Halbach magnetized permanent-magnet machines," *IEEE Transactions on Magnetics*, Vol. 40, No. 4, 2004, pp. 1864–1872. https://doi.org/10.1109/TMAG.2004.828933.

[23] Shen, Y., and Zhu, Z.-Q., "General analytical model for calculating electromagnetic performance of permanent magnet brushless machines having segmented Halbach array," *IET Electrical Systems in Transportation*, Vol. 3, No. 3, 2013, pp. 57–66. https://doi.org/https://doi.org/10.1049/iet-est.2012.0055, URL https://ietresearch.onlinelibrary.wiley.com/doi/abs/10.1049/iet-est.2012.0055.

[24] Angle, M., "Modeling, design and optimization of permanent magnet synchronous machines," Ph.D. thesis, Massachusetts Institute of Technology, 2016.

[25] *Recoma 35E*, Arnold Magnetic Technologies, 2017. URL https://www.arnoldmagnetics.com/wp-content/uploads/2017/10/Recoma-35E-160205-final.pdf.